Internal Dynamics Stabilization of Single-Phase Power Converters With Lyapunov-Based Automatic-Power-Decoupling Control

Huawei Yuan, *Student Member, IEEE*, Sinan Li, *Member, IEEE*, Siew-Chong Tan, *Senior Member, IEEE*, and S. Y. Ron Hui, *Fellow, IEEE*

***Abstract*—Single-phase power converters with the active pulsating-power-buffering (PPB) function are essentially highly coupled and nonlinear systems. Advanced control techniques are needed for this emerging class of converters to achieve fast transient response and large-signal stability. Existing control solutions are based on either 1) linear control techniques that are operating-point specific or 2) nonlinear control techniques that are generally topology-dependent. The proposed work is an evolved generalized feedback-linearization (FBL) control approach that incorporates the direct Lyapunov control method. The proposed control provides good stabilization of the internal dynamics of the system (which is unviable with FBL control) while still retaining all the best features of FBL control. A kind of single-phase power conversion system with active PPB is described. It is shown that FBL control naturally destabilizes the system and that the proposed control can globally stabilize the system under various operating conditions while yielding fast dynamics.**

***Index Terms*—Single-phase power conversion, active power decoupling, internal dynamics stabilization, Lyapunov-based control.**

I. Introduction

SINGLE-PHASE power converters with the active pulsating-power-buffering (PPB) function are promising candidates for achieving high power density, high energy efficiency, and high reliability (H^3) [1]−[4]. The H^3 features are particularly attractive for a wide range of applications, such as consumer electronics (laptop adapters and LED drivers), telecom (the power supply unit for data centers and servers), and renewable energy, where power density, efficiency, and reliability are of the uttermost figure-of-merits.

The basic operating principles of single-phase power conversion with active PPB can be explained using Fig. 1. As introduced in [5], this new derivative of single-phase converters incorporates a third ripple port (see C_b in Fig. 1). By allowing a large voltage ripple Δv_b across C_b through active PPB control, the required C_b can be significantly reduced for buffering the double-line-frequency imbalanced power, which is inherent in any single-phase converters [6]. The reduction of the required energy storage enables the elimination of conventional bulk dc-link capacitors (typically electrolytic capacitors, or E-caps) and allows more compact and reliable non-E-caps (e.g., film or ceramic capacitors) to be used in the system, thereby achieving high compactness and long service lifetime.

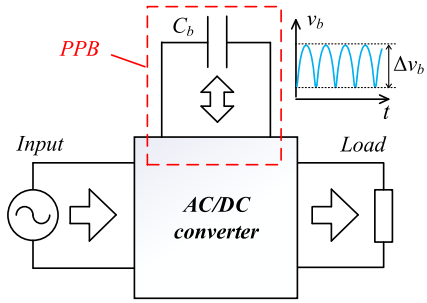

Fig. 1. Power conversion architecture of a single-phase PFC rectifier with active PPB.

There is a myriad of circuit configurations reported for single-phase power conversion with active PPB, showcasing superior power density (up to 200 W/in^3) and efficiency (up to 98%) [7]−[11]. Subsequently, advancement in the controller design is indispensable for attaining improved system-level performance. As reported in [5], H^3 converters are essentially highly nonlinear and coupled, and inherently involve a large-signal operation. Most of the existing control solutions, however, are linear control techniques that are valid only around specific operating points and do not take the nonlinearity and coupling effect into consideration. They are primarily targeted at narrow-load-range steady-state operations and are inapplicable to operations when fast response and large-signal stability are mandated [12]−[14]. In [4], a patent-pending nonlinear feedforward controller that provides excellent large-signal dynamic performance is proposed. However, the controller is topology-specific and the system's dynamic performance is not theoretically verified. In [5], a nonlinear control approach based on input-output feedback linearization (FBL) and an automatic-power-decoupling (APD) control strategy, namely FBL-APD control, was developed. The effectiveness of the controller was demonstrated with

Manuscript received January 18, 2019; revised April 10, 2019; accepted June 1, 2019. Date of publication June 5, 2019; date of current version November 12, 2019. This work was supported by the Hong Kong Research Grant Council under GRF Project 17205817. Recommended for publication by Associate Editor L. Corradini. *(Corresponding author: Sinan Li.)*

The authors are with the Department of Electrical and Electronic Engineering, The University of Hong Kong, Hong Kong (e-mail: hwyuan@connect.hku.hk; s.li@bath.ac.uk; sctan@eee.hku.hk; ronhui@eee.hku.hk).

Color versions of one or more of the figures in this paper are available online at http://ieeexplore.ieee.org

Digital Object Identifier 10.1109/TPEL.2019.2921416

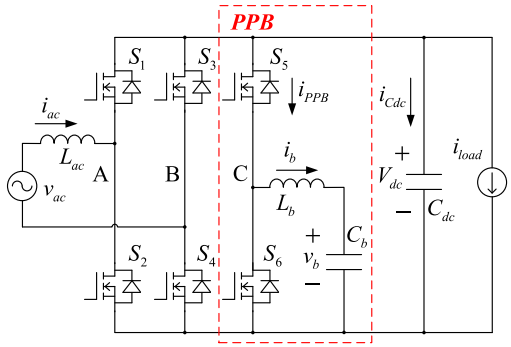

Fig. 2. Topology of the H^3 single-phase power converter with a buck-type PPB bridge leg.

the system's bandwidth and large-signal stability systematically derived and validated. The FBL-APD control is also applied to other recently proposed circuit configurations [15]−[19], demonstrating its versatility. Despite its effectiveness, FBL-APD control, as with other FBL controllers, possess a major limitation of being incapable of ensuring the stability of the system's internal dynamics, which are unobservable system states [20]. Therefore, the stability of a system with FBL-APD control is essentially determined by the stability of the internal dynamics and is system-dependent.

This study aims to complement the previously proposed FBL-APD controller by tackling the internal dynamics instability challenges. In particular, and for the first time, a Lyapunov-based APD (LP-APD) controller that can, actively stabilize the internal dynamics of the system while retaining all the advantages of FBL-APD control, such as fast dynamics and large-signal stability, is proposed. The proposed controller will be important in applications where the system's internal dynamics are unstable with an FBL-APD controller.

II. Mathematical Modeling and Steady-State Analysis of an H^3 Single-Phase Converter

The H^3 single-phase power converter topology investigated in this study is shown in Fig. 2. It comprises 1) a full-bridge active front end converter for ac/dc conversion and 2) a buck-type PPB bridge leg for removing the double-line-frequency voltage ripple from the dc-link [4], [5], [21]. Here, the PPB bridge leg operates in the continuous conduction mode (CCM) of operation and functions as a bidirectional buck/boost converter. Compared to the discontinuous conduction mode (DCM) of operation, a CCM PPB structure can achieve zero voltage switching by operating in the transition current mode [22], thereby enabling a higher-efficiency and higher-power-density design.

A. Mathematical Model of the H^3 Single-Phase Converter

The state-space-averaged model of the H^3 single-phase converter can be expressed as

$$\dot{\boldsymbol{x}} = \boldsymbol{f}(\boldsymbol{x}) + \boldsymbol{g}(\boldsymbol{x}) \cdot \boldsymbol{u} \tag{1}$$

where

$$\boldsymbol{x} = \begin{bmatrix} x_1 \\ x_2 \\ x_3 \\ x_4 \end{bmatrix} = \begin{bmatrix} i_{\rm ac} \\ v_{\rm dc} \\ i_b \\ v_b \end{bmatrix}, \ \boldsymbol{u} = \begin{bmatrix} u_1 \\ u_2 \end{bmatrix} = \begin{bmatrix} m \\ d_C \end{bmatrix}$$

$$\boldsymbol{f}(\boldsymbol{x}) = \begin{bmatrix} v_{\rm ac}/L_{\rm ac} \\ -i_{\rm load}/C_{\rm dc} \\ -v_b/L_b \\ i_b/C_b \end{bmatrix}, \ \boldsymbol{g}(\boldsymbol{x}) = \begin{bmatrix} -v_{\rm dc}/L_{ac} & 0 \\ i_{\rm ac}/C_{\rm dc} & -i_b/C_{\rm dc} \\ 0 & v_{dc}/L_b \\ 0 & 0 \end{bmatrix}. \tag{2}$$

Most of the variables in (2) are marked in Fig. 2. $u_1 = m$ is the modulation index of the full-bridge converter and $u_2 = d_C$ is the duty cycle of the PPB bridge leg. Both u_1 and u_2 are subject to the constraints

$$-1 < u_1 < 1, \ \ 0 < u_2 < 1. \tag{3}$$

Clearly, the mathematical model of the system described by (1) indicates that the system is highly nonlinear (due to the multiplication of $\boldsymbol{u}$ and $\boldsymbol{x}$) and highly coupled (between $\boldsymbol{u}$ and $\boldsymbol{x}$).

B. Steady-State Operation of the H^3 Single-Phase Converter

At steady state, the state-space model in (1) can be expressed as

$$\dot{\boldsymbol{x}}^{\boldsymbol{S}} = \boldsymbol{f}(\boldsymbol{x}^{\boldsymbol{S}}) + \boldsymbol{g}(\boldsymbol{x}^{\boldsymbol{S}}) \cdot \boldsymbol{u}^{\boldsymbol{S}} \tag{4}$$

where the variables with a superscript S represent their steady-state values.

Given that $v_{\rm ac}^S = V_{\rm AC}\sin(\omega t)$, $i_{\rm ac}^S = I_{\rm AC}\sin(\omega t)$, $v_{\rm dc}^S = V_{\rm od}$, and that $i_{\rm load}^S$ is a constant, the input power injected into the full-bridge converter is thus

$$\begin{aligned} P_{\rm in}^S &= \left(v_{\rm ac}^S - L_{\rm ac}\dot{i}_{\rm ac}^S\right) i_{\rm ac}^S \\ &= \frac{1}{2}V_{\rm AC}I_{\rm AC}\left[1 - \cos\left(2\omega t\right)\right] - \frac{1}{2}\omega L_{\rm ac}I_{\rm AC}^2\sin\left(2\omega t\right). \end{aligned} \tag{5}$$

The corresponding output power is

$$P_{\rm out}^S = v_{\rm dc}^S i_{\rm load}^S = V_{\rm od} i_{\rm load}^S. \tag{6}$$

Provided that inductance L_b is sufficiently small such that the energy stored in L_b is negligible, then the energy stored in the PPB circuit is

$$E_b^S = \frac{1}{2}C_b\left(v_b^S\right)^2. \tag{7}$$

Applying the principle of energy conservation to the converter, one has

$$\begin{aligned} \dot{E}_b^S &= P_{\rm in}^S - P_{\rm out}^S \\ &= -\frac{1}{2}V_{\rm AC}I_{\rm AC}\cos\left(2\omega t\right) - \frac{1}{2}\omega L_{\rm ac}I_{\rm AC}^2\sin\left(2\omega t\right) \end{aligned} \tag{8}$$

v_b^S can now be solved by combining (7) and (8), as

$$v_b^S = \sqrt{\frac{2E_{b0}}{C_b} - \frac{V_{\rm AC}I_{\rm AC}}{2\omega C_b}\sin\left(2\omega t\right) + \frac{L_{\rm ac}I_{\rm AC}^2}{2C_b}\cos\left(2\omega t\right)} \tag{9}$$

where E_{b0} is the initial energy of the PPB.

Substitution of (9) into (4) yields

$$i_b^S = C_b \dot{v}_b^S = \frac{-V_{\rm AC} I_{\rm AC} \cos(2\omega t) - \omega L_{\rm ac} I_{\rm AC}^2 \sin(2\omega t)}{2\sqrt{\frac{2E_{b0}}{C_b} - \frac{V_{\rm AC} I_{\rm AC}}{2\omega C_b}\sin(2\omega t) + \frac{L_{\rm ac} I_{\rm AC}^2}{2C_b}\cos(2\omega t)}}. \quad (10)$$

The expressions of $i_{\rm ac}^S$, i_b^S, and v_b^S indicate a large-signal operation with a small C_b even at the steady state.

$\boldsymbol{u}^S$ is directly solved from (4) as

$$u_1^S = \frac{v_{\rm ac}^S - L_{\rm ac}\dot{i}_{\rm ac}^S}{x_2^S}, u_2^S = \frac{u_1^S i_{\rm ac}^S - i_{\rm load}^S}{i_b^S} = \frac{v_b^S + L_b \dot{i}_b^S}{v_{\rm dc}^S}. \quad (11)$$

The complete time-domain expressions of u_1^S and u_2^S can finally be obtained by substituting $\boldsymbol{x^S}$ into (11).

III. Internal Dynamics Instability With Feedback-Linearization-Based APD Control

In [5], a nonlinear controller based on FBL-APD is proposed for the same H^3 converter in Fig. 2, except that the PPB operates in DCM. The controller successfully tackles the coupling and the nonlinearity issues of the system and achieves satisfactory steady-state and dynamic performances. However, as will be explained in the following, the same FBL-APD control is inapplicable when the PPB operates in CCM.

A. Review of FBL-APD Control

According to the APD control strategy, $i_{\rm ac}$ and $v_{\rm dc}$ are selected to form the control output vector $\boldsymbol{y}$, i.e.,

$$\boldsymbol{y} = \begin{bmatrix} y_1 \\ y_2 \end{bmatrix} = \begin{bmatrix} L_{\rm ac} i_{\rm ac} \\ C_{\rm dc} v_{\rm dc} \end{bmatrix}. \quad (12)$$

By following the FBL-APD control design procedure in [5], the decoupling control law can be derived as:

$$u_1 = \frac{v_{\rm ac} - v_1}{v_{\rm dc}}, \quad u_2 = \frac{u_1 i_{\rm ac} - v_2 - i_{\rm load}}{i_b}. \quad (13)$$

such that

$$\begin{bmatrix} \dot{y}_1 \\ \dot{y}_2 \end{bmatrix} = \begin{bmatrix} v_1 \\ v_2 \end{bmatrix} = \boldsymbol{v}. \quad (14)$$

$\boldsymbol{v}$ is a new set of control inputs, with which the original system model in (1) is decoupled and linearized.

If the feedback control law is designed as

$$v_1 = L_{\rm ac}\dot{i}_{\rm ac}^R + \alpha_1 \left(L_{\rm ac} i_{\rm ac}^R - y_1\right), \quad v_2 = \alpha_2 \left(C_{\rm dc} v_{\rm dc}^R - y_2\right) \quad (15)$$

with $i_{\rm ac}^R (= i_{\rm ac}^S)$ and $v_{\rm dc}^R (= v_{\rm dc}^S)$ being the references of $i_{\rm ac}$ and $v_{\rm dc}$, respectively, the error dynamics of the closed-loop system will be obtained from (14) and (15) as

$$\dot{e}_1 + \alpha_1 e_1 = 0 \quad (16)$$

$$\dot{e}_2 + \alpha_2 e_2 = 0 \quad (17)$$

where $e_1 = i_{\rm ac}^R - i_{\rm ac}$, $e_2 = v_{\rm dc}^R - v_{\rm dc}$, and α_i are design choices. Equations (16) and (17) suggest that 1) $i_{\rm ac}$ and $v_{\rm dc}$ have the simple first-order error dynamics in reference tracking, with bandwidths of $f_{BW1} = \alpha_1/2\pi$ and $f_{BW2} = \alpha_2/2\pi$, respectively, and 2) $i_{\rm ac}$ and $v_{\rm dc}$ are globally and exponentially stable, provided that $\alpha_1 > 0$ and $\alpha_2 > 0$.

B. Stability Analysis of the Internal Dynamics

With FBL-APD control, the dynamics of i_b and v_b are not directly controlled. The dynamics of the uncontrolled system states, also known as the internal dynamics, thus can easily affect the stability of the overall system. In the following analysis, it will be shown that the internal dynamics are actually unstable with the control law (13) and (15) despite that $i_{\rm ac}$ and $v_{\rm dc}$ have been stabilized.

The internal dynamics of the system are rewritten from (1) as

$$\dot{i}_b = -\frac{v_b}{L_b} + \frac{1}{L_b} v_{\rm dc} u_2 \quad (18)$$

$$\dot{v}_b = \frac{1}{C_b} i_b. \quad (19)$$

By substituting (13) into (18), the dynamics of i_b can be derived as

$$\dot{i}_b = -\frac{v_b}{L_b} + \frac{p_b}{L_b i_b}, \text{ or equivalently } L_b \dot{i}_b = -v_b + \frac{p_b}{i_b} \quad (20)$$

where $p_b = (v_{\rm ac} - v_1) i_{\rm ac} - v_2 v_{\rm dc} - i_{\rm load} v_{\rm dc}$.

According to (14), v_1 is the voltage drop across $L_{\rm ac}$ and v_2 is the current through $C_{\rm dc}$. Therefore, the physical meaning of p_b is precisely the instantaneous power absorbed by the PPB circuit. Equation (20) is the expected result as it is simply a Kirchhoff's voltage law (KVL) equation obtained with the PPB circuit, i.e., p_b/i_b is the average voltage at the node C (see Fig. 2), and $L_b \dot{i}_b$ and v_b are the voltages across L_b and C_b, respectively. Comparison of (18) and (20) shows that u_2 can also be expressed in terms of p_b as

$$u_2 = \frac{p_b}{v_{\rm dc} i_b}. \quad (21)$$

To simplify the analysis, zero dynamics are considered (i.e., when $e_1 = e_2 = 0$). Equation (20) is rewritten as

$$\dot{i}_b^Z = -\frac{v_b^Z}{L_b} + \frac{p_b^Z}{L_b i_b^Z} \quad (22)$$

with

$$p_b^Z = \left(v_{\rm ac} - L_{\rm ac}\dot{i}_{\rm ac}^R\right) i_{\rm ac}^R - i_{\rm load} v_{\rm dc}^R \quad (23)$$

where the variables with a superscript Z represent their zero dynamics.

On the other hand, by solving (3) and (18), the viable range of $\dot{i}_b^Z$ can be determined as

$$-\frac{v_b^Z}{L_b} < \dot{i}_b^Z < \frac{v_{\rm dc}^R - v_b^Z}{L_b}. \quad (24)$$

With (22) and (24), the phase plane of i_b^Z can be drawn. To simplify the analysis, it is assumed that $i_{\rm ac}^R$, v_b^Z, $v_{\rm ac}$, and $i_{\rm load}$

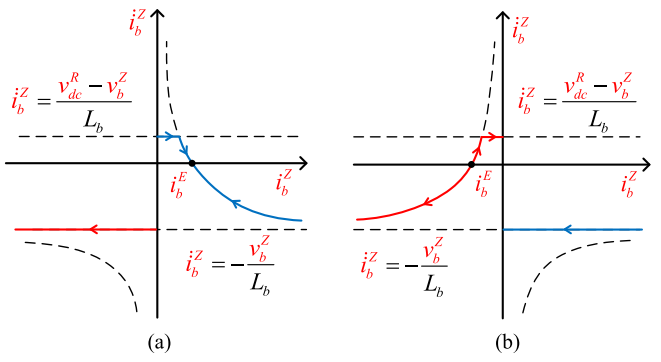

Fig. 3. Phase plane of x_3 when (a) $p_b^Z > 0$ and (b) $p_b^Z < 0$.

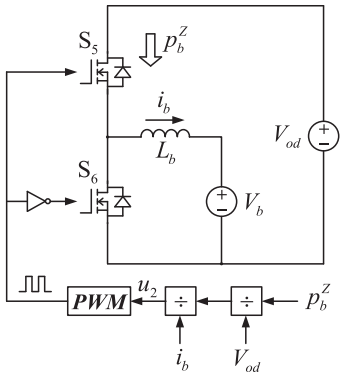

Fig. 4. Schematic diagram of the PPB circuit with the controller in the simulation.

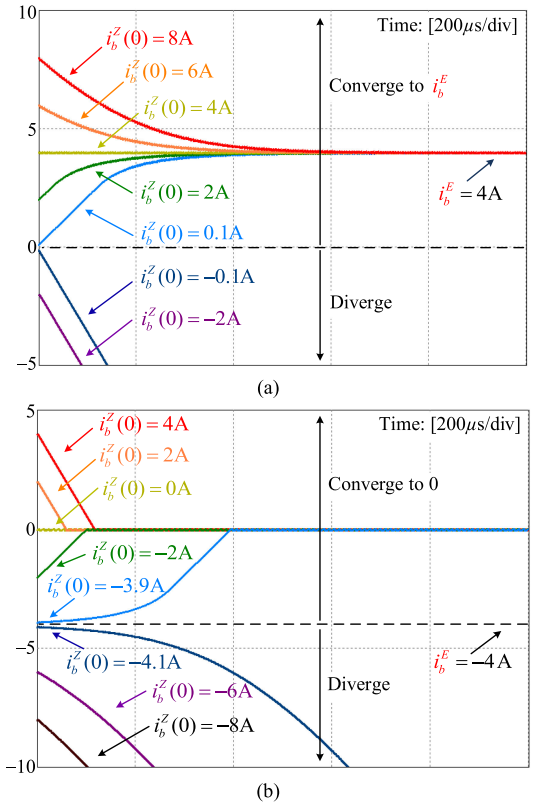

Fig. 5. Simulated time-domain responses of x_3^Z with (a) $p_b^Z = 1$ kW and (b) $p_b^Z = -1$ kW.

are constant. This is justified by the fact that the dynamics of i_b is significantly faster than the dynamics of $i_{\rm ac}^R$, v_b^Z, $v_{\rm ac}$, and $i_{\rm load}$ due to a small L_b. Furthermore, (23) indicates that p_b^Z can also be regarded as a constant. The phase plane of i_b is now drawn in Fig. 3 by considering the following two scenarios.

Scenario 1: When $p_b^Z > 0$, the PPB circuit is absorbing energy from the dc bus. By equating $\dot{i}_b^Z$ to zero in (22), the equilibrium point of i_b^Z is calculated as $i_b^E = p_b^Z / v_b^Z$, which is positive. Fig. 3(a) shows that i_b^Z will converge to i_b^E if $i_b^Z(0) > 0$ ($i_b^Z(0)$ is the initial value of i_b^Z), but will decrease unboundedly if $i_b^Z(0) < 0$, i.e., i_b^Z is merely locally stable.

Scenario 2: When $p_b^Z < 0$, the PPB circuit is injecting energy to the dc bus and i_b^E is negative. Fig. 3(b) indicates that i_b^Z will converge to zero if $i_b^Z(0) > i_b^E$, but will decrease unboundedly if $i_b^Z(0) < i_b^E$, i.e., i_b^Z is globally unstable.

The time-domain responses of i_b^Z given different $i_b^Z(0)$ are further simulated and the results are shown in Fig. 5. The simulation is conducted on the PPB circuit solely where C_b and $C_{\rm dc}$ are replaced by two voltage sources V_b and $V_{\rm od}$, respectively. The schematic diagram of the simulated PPB circuit [controlled according to (21)] is shown in Fig. 4, where $V_{\rm od} = 400$ V, $V_b = 250$ V, and p_b^Z is set as 1 kW and -1 kW for Scenario 1 and 2, respectively. From Fig. 5, the following observations can be made:

1) In Scenario 1, $i_b^E = 4$ A. Fig. 5(a) depicts that all the five curves with $i_b^Z(0) > 0$ converge to 4 A while the other two with $i_b^Z(0) < 0$ decrease unboundedly.
2) In Scenario 2, $i_b^E = -4$ A. Fig. 5(b) depicts that all the five curves with $i_b^Z(0) > -4$ A converge to zero while the other three with $i_b^Z(0) < -4$ A decrease unboundedly.

The simulation results are a good match with the above discussion.

The simulation waveforms of the overall system with FBL-APD control [according to (13) and (15)] are shown in Fig. 6. It is clearly noted that

a) the system's internal dynamics, i.e., v_b and i_b, are fluctuating significantly around their respective set points and are unstable;
b) the system's direct control outputs, i.e., $i_{\rm ac}$ and $v_{\rm dc}$, are also highly unstable as the instability of the internal dynamics severely distorts the reference for $i_{\rm ac}$ and turns the system into abnormal operation.

These simulated waveforms clearly demonstrate the incapability of the conventional FBL-APD control techniques when applied to control the target power converter.

IV. Proposed Nonlinear APD Control With Lyapunov Direct Method

Equation (18) shows that the internal dynamics of i_b is determined by u_2 only. To stabilize i_b, a different u_2 from that in (21)

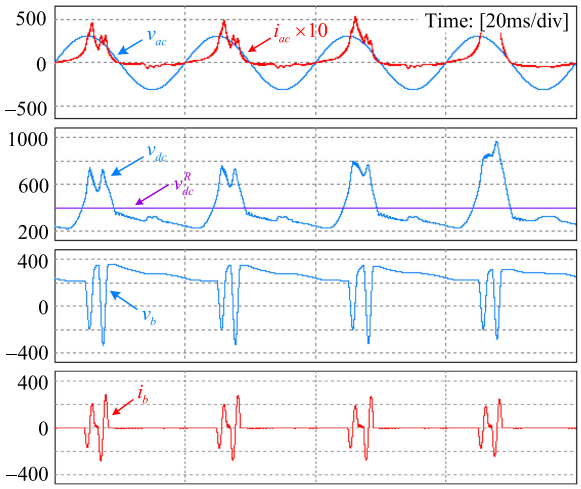

Fig. 6. Simulation waveforms of the system with FBL-APD control.

is needed. Modification of u_2 will not affect the dynamics of $i_{\rm ac}$ but will alter the dynamics of $v_{\rm dc}$ according to (1), meaning that the stability of $v_{\rm dc}$ is no longer guaranteed. It is therefore desirable to develop a new control law of u_2 that can ensure the stability of $v_{\rm dc}$ and i_b simultaneously while still retaining a simple first-order and decoupled dynamics of $v_{\rm dc}$ as that described in (17). This problem is to be addressed by the proposed Lyapunov-based APD (LP-APD) control described as follows.

A. Stabilization of v_{dc} and i_b

The LP-APD control uses a two-step approach to stabilize $v_{\rm dc}$ and i_b. First, the Lyapunov direct method is used to ensure that $v_{\rm dc}$ converges to $v_{\rm dc}^R$ and i_b to i_b^R (signified by $v_{\rm dc} \to v_{\rm dc}^R$ and $i_b \to i_b^R$). i_b^R is a virtual signal in a reference system, which we shall define shortly. Second, as $v_{\rm dc}^R = v_{\rm dc}^S$, $v_{\rm dc} \to v_{\rm dc}^S$ is obtained, verifying the stability of $v_{\rm dc}$. We then merely need to verify that $i_b^R \to i_b^S$ such that $i_b \to i_b^S$ and the stability of i_b is ensured.

1) Step 1: According to the Lyapunov stability theory [23]−[25], to ensure $v_{\rm dc} \to v_{\rm dc}^R$ and $i_b \to i_b^R$ (or $e_2 \to 0$ and $e_3 \to 0$), a Lyapunov function candidate $V(e_2, e_3)$ should be found.

Analogous to (18), we define a reference system as

$$\dot{i}_b^R = -\frac{v_b}{L_b} + \frac{1}{L_b} v_{\rm dc} u_2^R \tag{25}$$

where u_2^R is the duty ratio of the PPB bridge leg in the reference system.

Assuming that $L_b \dot{i}_b^R$ is sufficiently small, u_2^R is solved from (25) as

$$u_2^R = \frac{L_b \dot{i}_b^R + v_b}{v_{\rm dc}} \approx \frac{v_b}{v_{\rm dc}}. \tag{26}$$

The error dynamics of i_b is obtained by subtracting (18) from (25) as

$$\dot{e}_3 = \frac{1}{L_b} v_{\rm dc} e_{u2} \tag{27}$$

with

$$e_{u2} = u_2^R - u_2. \tag{28}$$

The functions of e_2 and e_3 are designed as $V(e_2, e_3) = V_1(e_2) + V_2(e_3)$ with $V_1(e_2) = 0.5 C_{\rm dc} e_2^2$, $V_2(e_3) = 0.5 L_b e_3^2$.

According to the Lyapunov's direct method, $(e_2, e_3) = (0, 0)$ is a globally stable operating point if $V(e_2, e_3)$ is a Lyapunov function candidate, i.e.,

$$\dot{V}(e_2, e_3) = \dot{V}_1(e_2) + \dot{V}_2(e_3) \le 0 \tag{29}$$

where

$$\dot{V}_1(e_2) = -C_{\rm dc} e_2 \dot{v}_{\rm dc} = e_2 \left[i_{\rm load} - \frac{i_{\rm ac}}{v_{\rm dc}} (v_{\rm ac} - v_1) + i_b u_2 \right] \tag{30}$$

$$\dot{V}_2(e_3) = L_b e_3 \dot{e}_3 = v_{dc} e_3 e_{u2}. \tag{31}$$

A sufficient condition for (29) is to achieve $\dot{V}_1(e_2) \le 0$ and $\dot{V}_2(e_3) \le 0$ simultaneously. It can be seen that if

$$e_{u2} = -\frac{\beta_1 e_3}{v_{\rm dc}} \tag{32}$$

with $\beta_1 > 0$, then $\dot{V}_2(e_3)$ will become

$$\dot{V}_2(e_3) = -\beta_1 e_3^2 \le 0. \tag{33}$$

Combination of (28) and (32) leads to

$$u_2 = u_2^R - e_{u2} = \frac{v_b + \beta_1 e_3}{v_{\rm dc}} = \frac{v_b + \beta_1 \left(i_b^R - i_b \right)}{v_{\rm dc}}. \tag{34}$$

By substituting u_2 into (30), $\dot{V}_1(e_2)$ is further obtained as

$$\begin{aligned} \dot{V}_1(e_2) &= -C_{\rm dc} e_2 \dot{v}_{\rm dc} \\ &= e_2 \left[\frac{v_{\rm dc} i_{\rm load} - (v_{\rm ac} - v_1) i_{\rm ac}}{v_{\rm dc}} + \left(\frac{v_b + \beta_1 e_3}{v_{\rm dc}} \right) i_b \right]. \end{aligned} \tag{35}$$

Provided that the dynamics of i_b is significantly faster than that of $v_{\rm dc}$ (referred to as *Condition A* hereafter), $i_b = i_b^R$ (or $e_3 = 0$) can be assumed in the calculation of $\dot{V}_1(e_2)$. Equation (35) then becomes

$$\dot{V}_1(e_2) = \frac{e_2}{v_{\rm dc}} \left[v_{\rm dc} i_{\rm load} - (v_{\rm ac} - v_1) i_{\rm ac} + v_b i_b^R \right]. \tag{36}$$

if

$$i_b^R = \frac{(v_{\rm ac} - v_1) i_{\rm ac} - i_{\rm load} v_{\rm dc} - \beta_2 v_{\rm dc} e_2}{v_b} \tag{37}$$

with $\beta_2 > 0$, $\dot{V}_1(e_2)$ will become

$$\dot{V}_1(e_2) = -\beta_2 e_2^2 \le 0. \tag{38}$$

Therefore, (29) is fulfilled, ensuring that $v_{\rm dc} \to v_{\rm dc}^R$ and $i_b \to i_b^R$.

2) Step 2: As we have proved above that $i_{\rm ac} \to i_{\rm ac}^S$, $v_{\rm dc} \to v_{\rm dc}^S$ and $i_b \to i_b^R$, (37) becomes

$$i_b^R = \frac{\left(v_{\rm ac}^S - L_{\rm ac} \dot{i}_{\rm ac}^S \right) i_{\rm ac}^S - v_{\rm dc}^S i_{\rm load}^S}{v_b} \tag{39}$$

at steady state. i_b^R can then be solved from (19) and (39) as

$$i_b^R = \frac{-V_{\rm AC} I_{\rm AC} \cos(2\omega t) - \omega L_{\rm ac} I_{\rm AC}^2 \sin(2\omega t)}{2\sqrt{\frac{2E_{b0}}{C_b} - \frac{V_{\rm AC} I_{\rm AC}}{2\omega C_b}\sin(2\omega t) + \frac{L_{\rm ac} I_{\rm AC}^2}{2C_b}\cos(2\omega t)}} = i_b^S \tag{40}$$

which is bounded. Therefore, together with the results in Step 1, we have proved that $v_{\rm dc}$ and i_b are stable and converge to their steady-state values, respectively, with the control laws of (34) and (37).

B. Dynamics Analysis of the Overall System

According to (1), the error dynamics of $i_{\rm ac}$ is only related to u_1. As u_1 needs no modification, the dynamics of $i_{\rm ac}$ is the same as (16), i.e.,

$$\dot{e}_1 + \alpha_1 e_1 = 0 \tag{41}$$

which is stable with a bandwidth of $f_{BW1} = \alpha_1/2\pi$.

The error dynamics of $v_{\rm dc}$ is obtained by substituting (34) and (37) into (1) as

$$\dot{e}_2 + \frac{\beta_2}{C_{\rm dc}} e_2 + \Delta = 0 \tag{42}$$

with

$$\Delta = \frac{1}{C_{\rm dc}}\left(\frac{\beta i_b}{v_b} - 1\right)\left(\beta_2 e_2 + i_{\rm load} + \frac{v_b i_b}{v_{\rm dc}} - u_1 i_{\rm ac}\right). \tag{43}$$

The error dynamics in (42) differs from that in (17) with an additional nonlinear term Δ, confirming that the dynamics of $v_{\rm dc}$ is altered with the LP-APD control.

However, notice that $\Delta \approx 0$ on *Condition A*. Thus by setting $\beta_2 = C_{\rm dc}\alpha_2$, (42) becomes

$$\dot{e}_2 + \alpha_2 e_2 = 0 \tag{44}$$

which is the same as (17). This result is highly favorable because it indicates that the first-order and decoupled dynamics of $v_{\rm dc}$ can still be approximately retained with the LP-APD control on *Condition A*.

The error dynamics of i_b is derived by substituting (32) into (27) as

$$\dot{e}_3 + \frac{\beta_1}{L_b} e_3 = 0 \tag{45}$$

which again describes a first-order response with a bandwidth of $f_{BW3} = \beta_1/2\pi L_b$.

Condition A can, therefore, be achieved by selecting appropriate α_2 and β_1 such that

$$\frac{\alpha_2}{2\pi} \ll \frac{\beta_1}{2\pi L_b} \text{ or } \beta_1 \gg \alpha_2 L_b \tag{46}$$

Finally, according to (19), the error dynamics of v_b is

$$\dot{e}_4 = \frac{1}{C_b} e_3. \tag{47}$$

As $i_{\rm ac} \to i_{\rm ac}^S$, $v_{\rm dc} \to v_{\rm dc}^S$, $i_b \to i_b^S$ at steady state, we can conclude that $v_b \to v_b^S$ according to the principle of conservation of energy, and that v_b is stable.

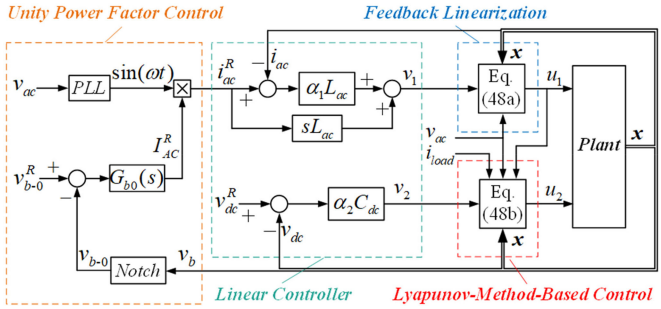

Fig. 7. Overall schematic diagram of the proposed LP-APD control including unity power factor control.

The complete control law of the proposed LP-APD control is summarized as

$$u_1 = \frac{v_{\rm ac} - v_1}{v_{\rm dc}} \tag{48a}$$

$$u_2 = \frac{v_b + \beta_1 e_3}{v_{\rm dc}} = \frac{\beta_1(u_1 i_{\rm ac} - v_2 - i_{\rm load})}{v_b} + \frac{v_b - \beta_1 i_b}{v_{\rm dc}} \tag{48b}$$

with v_1 and v_2 given in (15). Fig. 7 depicts the overall control schematic diagram with the unity power factor control included.

C. Design Considerations

To present a more comprehensive evaluation of the proposed controller in a practical setting, the impacts of component tolerances on the controller performance are analyzed. For simplicity, the above representations, i.e., $L_{\rm ac}$, $C_{\rm dc}$, L_b, C_b, are reused to denote the exact values of these parameters, while their respective measurements are signified as $\hat{L}_{ac}$, $\hat{C}_{\rm dc}$, $\hat{L}_b$, $\hat{C}_b$ with

$$\hat{L}_{\rm ac} = L_{\rm ac} + \Delta L_{\rm ac}, \quad \hat{C}_{\rm dc} = C_{\rm dc} + \Delta C_{\rm dc}$$
$$\hat{L}_b = L_b + \Delta L_b, \quad \hat{C}_b = C_b + \Delta C_b. \tag{49}$$

Then the proposed control law alters from (48) to

$$u_1 = \frac{v_{\rm ac} - \hat{L}_{\rm ac}\dot{i}_{\rm ac}^R - \alpha_1 \hat{L}_{\rm ac} e_1}{v_{\rm dc}}$$
$$u_2 = \frac{\beta_1\left(u_1 i_{\rm ac} - \alpha_2 \hat{C}_{\rm dc} e_2 - i_{\rm load}\right)}{v_b} + \frac{v_b - \beta_1 i_b}{v_{\rm dc}}. \tag{50}$$

Substituting (50) into (1) gives the system's actual dynamics

$$\dot{i}_{\rm ac} = \frac{\hat{L}_{\rm ac}}{L_{\rm ac}}\dot{i}_{\rm ac}^R + \frac{\hat{L}_{\rm ac}}{L_{\rm ac}}\alpha_1 e_1 \quad \dot{v}_{\rm dc} = \frac{\hat{C}_{\rm dc}}{C_{\rm dc}}\alpha_2 e_2$$
$$\dot{i}_b = \frac{\beta}{L_b} e_3 \quad \dot{v}_b = \frac{1}{C_b} i_b \tag{51}$$

TABLE I
IMPACTS OF PARAMETER UNCERTAINTIES ON CONTROLLER PERFORMANCE

Parameter	Impacts of Component Tolerances
L_{ac}	1. Bandwidth of x_1 control loop: $f_{BW1}=\frac{\hat{L}_{ac}}{L_{ac}}\cdot\hat{f}_{BW1}$
	2. Steady-state error of x_1: $-I_{dLac}\sin(\omega t+\theta)$
C_{dc}	Bandwidth of x_2 control loop: $f_{BW2}=\frac{\hat{C}_{dc}}{C_{dc}}\cdot\hat{f}_{BW2}$
L_b	Bandwidth of x_3 control loop: $f_{BW3}=\frac{\hat{L}_b}{L_b}\cdot\hat{f}_{BW3}$
C_b	No impact.

TABLE II
SPECIFICATIONS OF THE SYSTEM IN SIMULATION AND EXPERIMENTS

Parameter		Simulation	Experiment
Rated power		2 kW	300 W
Switching frequency		25 kHz	25 kHz
Ac port	v_{ac}	220 V (RMS) / 50 Hz	220 V (RMS) / 50 Hz
	L_{ac}	1 mH	7 mH
Dc port	V_{dc}	400 V	400 V
	C_{dc}	20 μF	20 μF
Ripple port	C_b	200 μF	50 μF
	L_b	0.3 mH	1.87 mH
Controller Coefficients	f_{BW1}	2.5 kHz	2.5 kHz
	f_{BW2}	400 Hz	400 Hz
	f_{BW3}	2 kHz	2 kHz

e_1 is solved from (51) as

$$e_1 = e_1(0)\cdot e^{-\frac{\hat{L}_{\rm ac}}{L_{\rm ac}}\cdot\alpha_1 t} - \frac{\Delta L_{\rm ac}}{L_{\rm ac}}\frac{\omega L_{\rm ac} I_{\rm AC}}{\sqrt{(\omega L_{\rm ac})^2+(\alpha_1\hat{L}_{\rm ac})^2}} \times \sin\left(\omega t+\arctan\left(\frac{\alpha_1\hat{L}_{\rm ac}}{\omega L_{\rm ac}}\right)\right). \quad (52)$$

Equation (52) shows that e_1 comprises two parts, one related to the initial error $e_1(0)$ and the other one caused by inaccurate knowledge of $L_{\rm ac}$. The latter part is generally very small in magnitude owing to small $\Delta L_{\rm ac}/L_{\rm ac}$ and large α_1/ω, while the former part will dissipate exponentially with a bandwidth of

$$f_{BW1} = \frac{\hat{L}_{\rm ac}}{L_{\rm ac}}\cdot\frac{\alpha_1}{2\pi} = \frac{\hat{L}_{\rm ac}}{L_{\rm ac}}\cdot\hat{f}_{BW1} \quad (53)$$

where $\hat{f}_{BW1}$ represents the designed bandwidth of the $i_{\rm ac}$ control loop.

Similarly, the impacts of the uncertainties of $C_{\rm dc}$, L_b, C_b can also be analyzed quantitatively. The results are summarized in Table I.

V. SIMULATIONS AND EXPERIMENTAL RESULTS

To examine the performance of the proposed LP-APD control, a 2-kW model of the H^3 single-phase converter was first simulated in PSIM and a downsized 300-W prototype was also constructed. The system's specifications in both the simulation and the experiments are listed in Table II. In particular, the bandwidths of the controller in both cases are designed identical as $f_{BW1}=2.5$ kHz, $f_{BW2}=400$ Hz, $f_{BW3}=2$ kHz.

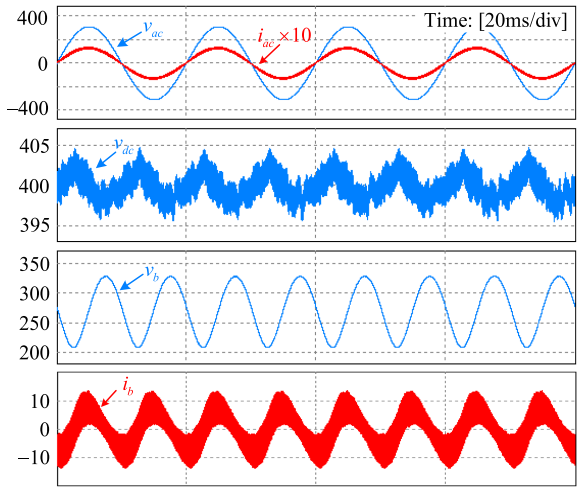

Fig. 8. Steady-state waveforms of the system with the proposed LP-APD control.

A. Simulation Verification

1) Steady-State Performance: The steady-state waveforms of the proposed LP-APD controller are illustrated in Fig. 8. At the input port, the waveform of $i_{\rm ac}$ has a low total harmonic distortion (THD) of 0.6% and almost no phase displacement with respect to $v_{\rm ac}$, testifying a good regulation of $i_{\rm ac}$ and a unity power factor. At the output port, $v_{\rm dc}$ is regulated at 400 V with a peak-to-peak ripple of about 9 V (2.3%). The instantaneous power difference between the input and the output is buffered by the PPB, leading to a large-signal voltage variation of v_b in Fig. 8. Finally, the waveform of i_b confirms CCM operation of the PPB.

2) Transient Performance: First, step-up/down changes of $i_{\rm ac}^R$, $v_{\rm dc}^R$ and i_b^R (i.e., x_1^R, x_2^R and x_3^R) are conducted to verify the control bandwidth design analysis in Section IV-B. The results are displayed in Fig. 8. First-order responses of $i_{\rm ac}$, $v_{\rm dc}$ and i_b can be clearly observed from Fig. 9 for both reference step-up and step-down. The respective settling times of $i_{\rm ac}$, $v_{\rm dc}$ and i_b are measured in Fig. 9 to be around 300 μs, 1 ms and 300 μs, which are very close to their theoretical values of 318 μs, 2.0 ms and 398 μs. Note that the slight differences between the estimated and the theoretical settling time are mainly due to 1) the large switching ripple of i_b, 2) the double-line-frequency ripple of $v_{\rm dc}$, 3) the time-varying nature of $i_{\rm ac}^R$ and i_b^R. These disturbances make precise estimation of the settling time difficult.

Second, load step change tests are carried out, and the waveforms are displayed in Fig. 10. In Fig. 10(a), a negative spike of 23 V appears in $v_{\rm dc}$ as the load steps up from 0 to 2 kW. With the proposed LP-APD controller, $v_{\rm dc}$ quickly recovers and settles back to its reference 400 V within 1 ms. In Fig. 10(b), a positive spike of 21 V in $v_{\rm dc}$ is observed due to sudden load removal and the fast response of $v_{\rm dc}$ is also demonstrated.

B. Experimental Results

1) Steady-State Performance: Fig. 11 shows the steady-state operating waveforms of the power converter at the input port, the

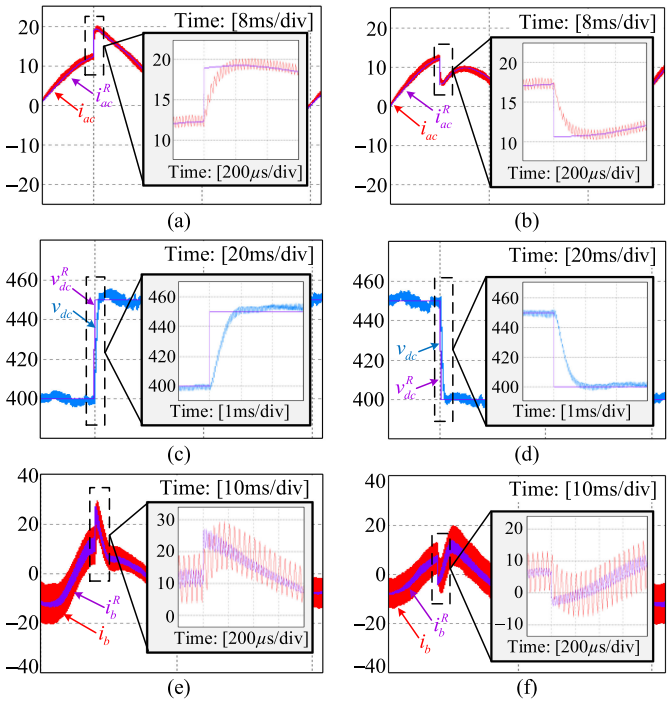

Fig. 9. Transient waveforms with the proposed LP-APD control in the tests of (a) step-up change of $i_{\rm ac}^R$, (b) step-down change of $i_{\rm ac}^R$, (c) step-up change of $v_{\rm dc}^R$, (d) step-down change of $v_{\rm dc}^R$, (e) step-up change of i_b^R, and (f) step-down change of i_b^R.

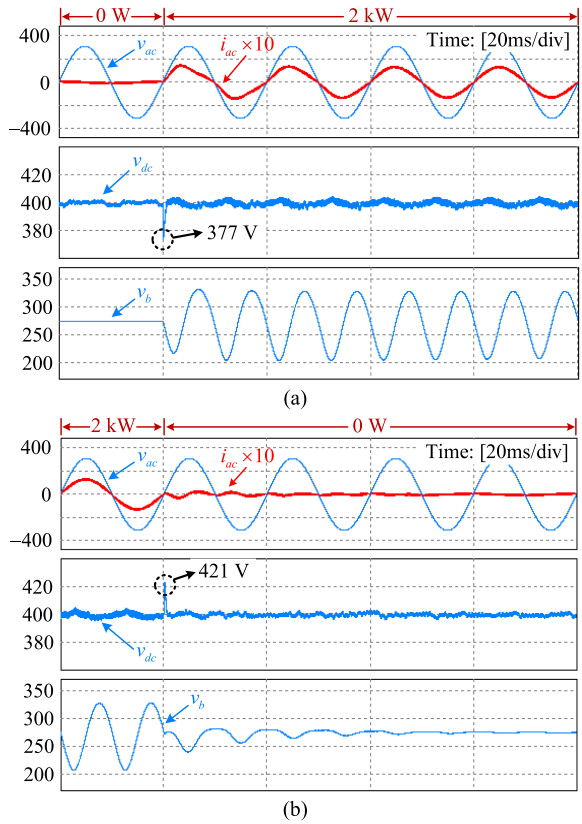

Fig. 10. Transient waveforms of the system in the processes of (a) load step up and (b) load step down.

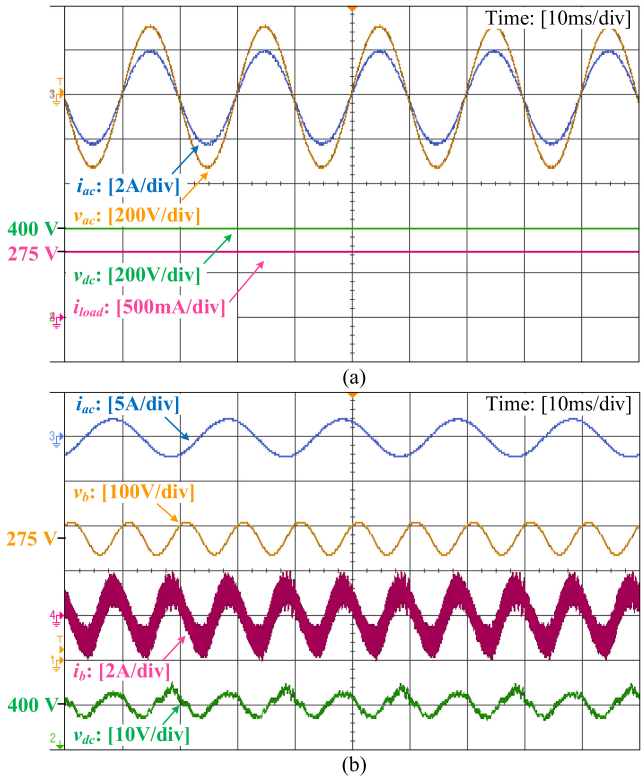

Fig. 11. Steady-state waveforms of the system with the proposed LP-APD control at 300-W output power at (a) the ac- and the dc-port and (b) the ripple-port.

output port, and the ripple port with the proposed LP-APD control at full load (300 W). All the waveforms in Fig. 11 match well with the simulation results in Fig. 8. The THD of $i_{\rm ac}$ is measured at 2.21% and the peak-to-peak ripple voltage of $v_{\rm dc}$ is measured at 8 V (2% of the average $v_{\rm dc}$), demonstrating good regulations of the line current and the output voltage. The stability of the internal dynamics, i.e., i_b, is also confirmed.

2) Transient Performance: Fig. 12 depicts the dynamic responses of the system as the load is step changed between 0 and 300 W. Fig. 12(a) illustrates that $v_{\rm dc}$ is almost immune to the step-up load change and remains its tight regulation at 400 V. As a sudden increase of the output power leads to a sudden power imbalance between the input and output, the buffer energy in the PPB circuit is released to the dc bus immediately to compensate the power imbalance [see v_b in Fig. 12(a)] in an automatic fashion, similar to the result in [5]. The fast responses and robustness of the proposed control are also validated by Fig. 12(b) as the load is suddenly cut off.

Fig. 13 further illustrates the transient waveforms of the converter as the output voltage reference is changed between 380 and 420 V. $v_{\rm dc}$ is shown to have a fast response and follow a typical first-order response. The settling time of $v_{\rm dc}$ is around 2 ms, which is a good match to both the theoretical value (2 ms) and the simulation result (1 ms) in Fig. 9. Additionally, the fast response of $i_{\rm ac}$ and the PPB function are also demonstrated in Fig. 13.

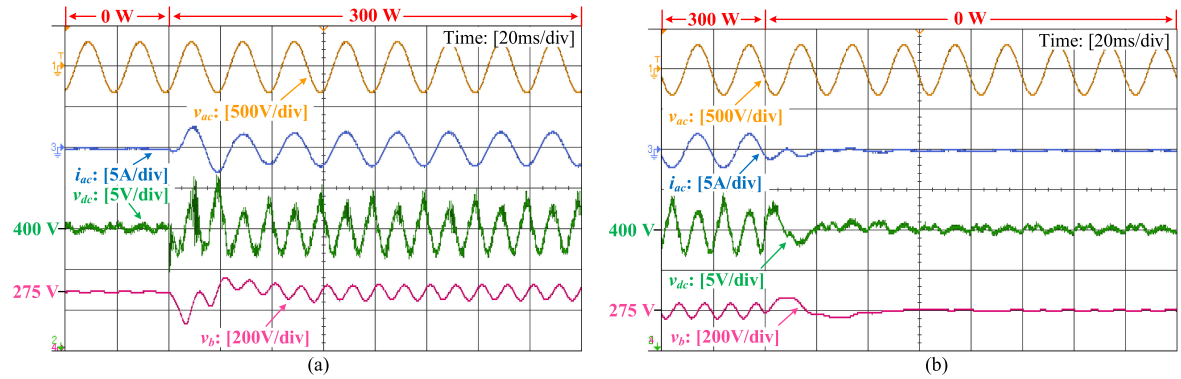

Fig. 12. Transient waveforms of the system with the proposed LP-APD control as the output power changes (a) from 0 to 300 W and (b) from 300 to 0 W.

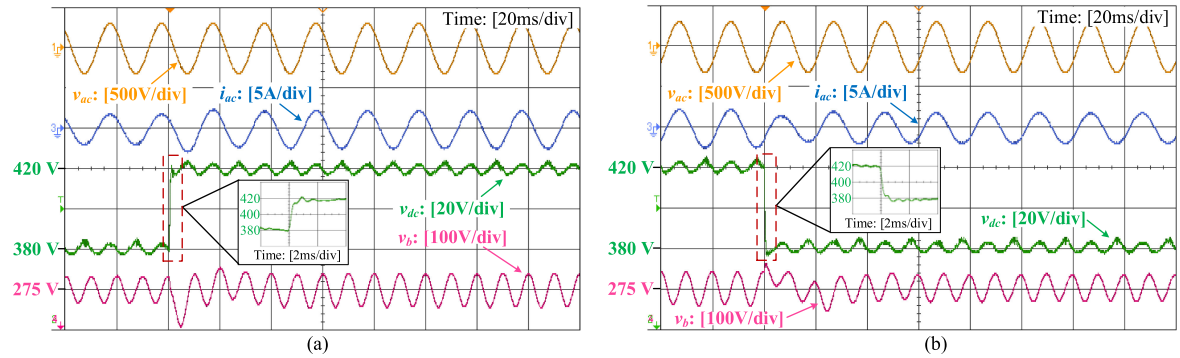

Fig. 13. Transient waveforms of the system with the proposed LP-APD control as the output voltage reference changes (a) from 380 to 420 V and (b) from 420 to 380 V.

VI. Conclusion

In this study, the control of single-phase power converters that possess the active PPB function is investigated. A prior-art generalized nonlinear controller that combines the FBL theory and the APD control strategy, or an FBL-APD controller, is applied to a type of single-phase converters with active PPB. The internal dynamics instability phenomenon is demonstrated both mathematically and using simulations. To solve the instability problem, an evolved FBL-APD controller that incorporates the direct Lyapunov control method, or an LP-APD controller, is proposed, where the system's internal dynamics are utilized to formulate the Lyapunov energy function $V(x)$. Theoretical analysis is presented to show that the proposed LP-APD control can well stabilize the internal dynamics while still retaining the best features of the FBL-APD control. Simulation and experimental waveforms successfully confirm the feasibility of this new control approach. The proposed control technique, as a complement of the generalized FBL-APD control, can be very useful for controlling emerging single-phase converters with active PPB while enriching the existing FBL control theory.

References

[1] P. T. Krein and R. S. Balog, "Cost-effective hundred-year life for single-phase inverters and rectifiers in solar and LED lighting applications based on minimum capacitance requirements and a ripple power port," in *Proc. 24th Annu. IEEE Appl. Power Electron. Conf. Expo.*, Washington, DC, USA, 2009, pp. 620–625.

[2] R. Wang *et al.*, "A high power density single-phase PWM rectifier with active ripple energy storage," *IEEE Trans. Power Electron.*, vol. 26, no. 5, pp. 1430–1443, May 2011.

[3] S. Wang, X. Ruan, K. Yao, S. C. Tan, Y. Yang, and Z. Ye, "A flicker-free electrolytic capacitor-less ac–dc LED driver," *IEEE Trans. Power Electron.*, vol. 27, no. 11, pp. 4540–4548, Nov. 2012.

[4] D. Neumayr, D. Bortis, and J. W. Kolar, "Ultra-compact power pulsation buffer for single-phase dc/ac converter systems," in *Proc. IEEE 8th Int. Power Electron. Motion Control Conf.*, Hefei, China, 2016, pp. 2732–2741.

[5] H. Yuan, S. Li, W. Qi, S. C. Tan, and S. Y. R. Hui, "On nonlinear control of single-phase converters with active power decoupling function," *IEEE Trans. Power Electron.*, vol. 34, no. 6, pp. 5903–5915, Jun. 2019.

[6] P. T. Krein, R. S. Balog, and M. Mirjafari, "Minimum energy and capacitance requirements for single-phase inverters and rectifiers using a ripple port," *IEEE Trans. Power Electron.*, vol. 27, no. 11, pp. 4690–4698, Nov. 2012.

[7] S. Qin, Y. Lei, C. Barth, W. Liu, and R. C. N. Pilawa-Podgurski, "A high power density series-stacked energy buffer for power pulsation decoupling in single-phase converters," *IEEE Trans. Power Electron.*, vol. 32, no. 6, pp. 4905–4924, Jun. 2017.

[8] Y. Lei *et al.*, "A 2-kW single-phase seven-level flying capacitor multilevel inverter with an active energy buffer," *IEEE Trans. Power Electron.*, vol. 32, no. 11, pp. 8570–8581, Nov. 2017.

[9] Y. Lei *et al.*, "A 2 kW, single-phase, 7-level, GaN inverter with an active energy buffer achieving 216 W/in3 power density and 97.6% peak efficiency," in *Proc. IEEE Appl. Power Electron. Conf. Expo.*, Long Beach, CA, USA, 2016, pp. 1512–1519.

[10] J. W. Kolar, D. Bortis, and D. Neumayr, "The ideal switch is not enough," in *Proc. 28th Int. Symp. Power Semicond. Devices ICs*, Prague, Czech Republic, 2016, pp. 15–22.

[11] S. Li, G. Zhu, S. C. Tan, and S. Y. R. Hui, "Direct ac/dc rectifier with mitigated low-frequency ripple through inductor-current waveform control," *IEEE Trans. Power Electron.*, vol. 30, no. 8, pp. 4336–4348, Aug. 2015.

[12] H. Li, K. Zhang, H. Zhao, S. Fan, and J. Xiong, "Active power decoupling for high-power single-phase PWM rectifiers," *IEEE Trans. Power Electron.*, vol. 28, no. 5, pp. 1308–1319, Mar. 2013.

[13] M. Su, P. Pan, X. Long, Y. Sun, and J. Yang, "An active power-decoupling method for single-phase ac-dc converters," *IEEE Trans. Ind. Inform.*, vol. 10, no. 1, pp. 461–468, Feb. 2014.
[14] S. Li, W. Qi, S. C. Tan, and S. Y. R. Hui, "A single-stage two-switch PFC rectifier with wide output voltage range and automatic ac ripple power decoupling," *IEEE Trans. Power Electron.*, vol. 32, no. 9, pp. 6971–6982, Sep. 2017.
[15] S. Li, W. Qi, S. C. Tan, and S. Y. R. Hui, "Enhanced automatic-power-decoupling control method for single-phase ac-to-dc converters," *IEEE Trans. Power Electron.*, vol. 33, no. 2, pp. 1816–1828, Feb. 2018.
[16] H. Sun, H. Wang, and W. Qi, "Automatic power decoupling controller of dependent power decoupling circuit for enhanced transient performance," *IEEE Trans. Ind. Electron.*, vol. 66, no. 3, pp. 1820–1831, Mar. 2019.
[17] W. Qi, S. Li, S. C. Tan, and S. Y. R. Hui, "A single-phase three-level flying-capacitor PFC rectifier without electrolytic capacitors," *IEEE Trans. Power Electron.*, vol. 34, no. 7, pp. 6411–6424, Jul. 2019.
[18] K. Ding, Y. Zhang, J. Liu, X. Cheng, P. Zeng, and Y. Huang, "Single-phase ac-dc buck PFC converter based on flying-capacitor topology with active power decoupling control," in *Proc. IEEE Energy Convers. Congr. Expo.*, Portland, OR, USA, 2018, pp. 2885–2889.
[19] Y. Liu, Y. Sun, M. Su, M. Zhou, Q. Zhu, and X. Li, "A single-phase PFC rectifier with wide output voltage and low-frequency ripple power decoupling," *IEEE Trans. Power Electron.*, vol. 33, no. 6, pp. 5076–5086, Jun. 2018.
[20] J.-J. E. Slotine, and W. Li, "Feedback linearization" in *Applied Nonlinear Control*, vol. 199, 6th ed. Englewood Cliffs, NJ, USA: Prentice-Hall, 1991, pp. 216–228.
[21] O. Bomboir *et al.*, "Red electrical devils by CE+T team: Technical approach document," CE+T Power co., Liege, Belgium, Tech. Rep. 545-9151f5-56568, 2015.
[22] C. Marxgut, J. Biela, and J. W. Kolar, "Interleaved triangular current mode (TCM) resonant transition, single phase PFC rectifier with high efficiency and high power density," in *Proc. IEEE Int. Power Electron. Conf.*, Sapporo, Japan, 2010, pp. 1725–1732.
[23] S. R. Sanders and G. C. Verghese, "Lyapunov-based control for switched power converters," *IEEE Trans. Power Electron.*, vol. 7, no. 1, pp. 17–24, Jan. 1992.
[24] H. Komurcugil and O. Kukrer, "A new control strategy for single-phase shunt active power filters using a Lyapunov function," *IEEE Trans. Ind. Electron.*, vol. 53, no. 1, pp. 305–312, Feb. 2006.
[25] C. Meza, D. Biel, D. Jeltsema, and J. M. A. Scherpen, "Lyapunov-based control scheme for single-phase grid-connected PV central inverters," *IEEE Trans. Control Syst. Technol.*, vol. 20, no. 2, pp. 520–529, Mar. 2012.

Huawei Yuan (S'16) received the B.S. and M.S. degrees in electrical engineering from Tsinghua University, Beijing, China, in 2013 and 2016, respectively. He is currently working toward the Ph.D. degree at the Department of Electrical and Electronic Engineering, the University of Hong Kong, Hong Kong.

His current research interests include control of power converters and renewable energy.

Sinan Li (M'14) received the B.S. degree in electrical engineering from the Harbin Institute of Technology, Harbin, China, and the Ph.D. degree in electrical and electronic engineering from The University of Hong Kong, Hong Kong.

He is currently an Assistant Professor with the Department of Electronic and Electrical Engineering, The University of Bath, Bath, U.K. He has authored/coauthored more than 43 transaction papers and conference papers, and holds five U.S. patents. His research interests include all areas of power electronics.

Dr. Li is a founding member of IEEE-Eta Kappa Nu (HKN) at Hong Kong University.

Siew-Chong Tan (M'06–SM'11) received the B.Eng. (Hons.) and M.Eng. degrees in electrical and computer engineering from the National University of Singapore, Singapore, in 2000 and 2002, respectively, and the Ph.D. degree in electronic and information engineering from the Hong Kong Polytechnic University, Hong Kong, in 2005.

He is currently a Professor with the Department of Electrical and Electronic Engineering, The University of Hong Kong, Hong Kong. He was a Visiting Scholar with the Grainger Center for Electric Machinery and Electromechanics, University of Illinois at Urbana-Champaign, Champaign, IL, USA, from September to October 2009, and an Invited Academic Visitor of the Huazhong University of Science and Technology, Wuhan, China, in December 2011. He is a coauthor of the book *Sliding Mode Control of Switching Power Converters: Techniques and Implementation* (CRC, 2011). His research interests include power electronics and control, LED lightings, smart grids, and clean energy technologies.

Prof. Tan serves as an Associate Editor of the IEEE TRANSACTIONS ON POWER ELECTRONICS.

S. Y. Ron Hui (M'87–SM'94–F'03) received the B.Sc. (Hons.) Eng. degree in electrical and electronic engineering from the University of Birmingham, Birmingham, U.K., in 1984 and the D.I.C. and Ph.D. degrees from Imperial College London, London, U.K., in 1987.

Since July 2010, he has been concurrently a part-time Chair Professor of power electronics at Imperial College London and Philip Wong Wilson Wong Professor at The University of Hong Kong, Pokfulam, Hong Kong. He has authored and coauthored more than 270 refereed journal publications and book chapters, and more than 60 of his patents have been adopted by industry.

Dr. Hui is a Fellow of the Australian Academy of Technological Sciences and Engineering, the U.S. National Academy of Inventors, and also the Royal Academy of Engineering (U.K.). He is an Associate Editor of the IEEE TRANSACTIONS ON POWER ELECTRONICS and IEEE TRANSACTIONS ON INDUSTRIAL ELECTRONICS. He is an Editor of the IEEE JOURNAL OF EMERGING AND SELECTED TOPICS IN POWER ELECTRONICS. He was the recipient of the 2010 IEEE Rodulf Chope R&D Award, 2010 IET Crompton Medal, and 2015 IEEE William E. Newell Power Electronics Award.